3D shape of asteroid (6) Hebe from VLT/SPHERE imaging: Implications for the origin of ordinary H chondrites

M. Marsset, B. Carry, C. Dumas, J. Hanus, M. Viikinkoski, P. Vernazza, Müller T.G., M. Delbo, E. Jehin, M. Gillon, et al.

A&A 604, A64 (2017)
DOI: 10.1051/0004-6361/201731021

Astronomy & Astrophysics

3D shape of asteroid (6) Hebe from VLT/SPHERE imaging: Implications for the origin of ordinary H chondrites⋆

M. Marsset[1], B. Carry[2,3], C. Dumas[4], J. Hanuš[5], M. Viikinkoski[6], P. Vernazza[7], T. G. Müller[8], M. Delbo[2], E. Jehin[9], M. Gillon[9], J. Grice[2,10], B. Yang[11], T. Fusco[7,12], J. Berthier[3], S. Sonnett[13], F. Kugel[14], J. Caron[14], and R. Behrend[14]

[1] Astrophysics Research Centre, Queen's University Belfast, BT7 1NN, UK
e-mail: michael.marsset@qub.ac.uk
[2] Université Côte d'Azur, Observatoire de la Côte d'Azur, 06304 Lagrange, CNRS, France
[3] IMCCE, Observatoire de Paris, PSL Research University, CNRS, Sorbonne Universités, UPMC Univ Paris 06, Univ. Lille, France
[4] TMT Observatory, 100 W. Walnut Street, Suite 300, Pasadena, CA 91124, USA
[5] Astronomical Institute, Faculty of Mathematics and Physics, Charles University, V Holešovičkách 2, 18000 Prague, Czech Republic
[6] Department of Mathematics, Tampere University of Technology, PO Box 553, 33101 Tampere, Finland
[7] Aix Marseille Univ, CNRS, LAM, Laboratoire d'Astrophysique de Marseille, 13013 Marseille, France
[8] Max-Planck-Institut für extraterrestrische Physik, Giessenbachstrasse, 85748 Garching, Germany
[9] Space sciences, Technologies and Astrophysics Research Institute, Université de Liège, Allée du 6 Août 17, 4000 Liège, Belgium
[10] Open University, School of Physical Sciences, The Open University, MK7 6AA, UK
[11] European Southern Observatory (ESO), Alonso de Córdova 3107, 1900 Casilla Vitacura, Santiago, Chile
[12] ONERA – the French Aerospace Lab, 92322 Châtillon, France
[13] Planetary Science Institute, 1700 East Fort Lowell, Suite 106, Tucson, AZ 85719, USA
[14] CdR & CdL Group: Lightcurves of Minor Planets and Variable Stars, Observatoire de Genève, 1290 Sauverny, Switzerland

Received 22 April 2017 / Accepted 19 May 2017

ABSTRACT

Context. The high-angular-resolution capability of the new-generation ground-based adaptive-optics camera SPHERE at ESO VLT allows us to assess, for the very first time, the cratering record of medium-sized ($D \sim$ 100–200 km) asteroids from the ground, opening the prospect of a new era of investigation of the asteroid belt's collisional history.
Aims. We investigate here the collisional history of asteroid (6) Hebe and challenge the idea that Hebe may be the parent body of ordinary H chondrites, the most common type of meteorites found on Earth (~34% of the falls).
Methods. We observed Hebe with SPHERE as part of the science verification of the instrument. Combined with earlier adaptive-optics images and optical light curves, we model the spin and three-dimensional (3D) shape of Hebe and check the consistency of the derived model against available stellar occultations and thermal measurements.
Results. Our 3D shape model fits the images with sub-pixel residuals and the light curves to 0.02 mag. The rotation period (7.274 47 h), spin (ECJ2000 λ, β of 343°, +47°), and volume-equivalent diameter (193 ± 6 km) are consistent with previous determinations and thermophysical modeling. Hebe's inferred density is 3.48 ± 0.64 g cm^{-3}, in agreement with an intact interior based on its H-chondrite composition. Using the 3D shape model to derive the volume of the largest depression (likely impact crater), it appears that the latter is significantly smaller than the total volume of close-by S-type H-chondrite-like asteroid families.
Conclusions. Our results imply that (6) Hebe is not the most likely source of H chondrites. Over the coming years, our team will collect similar high-precision shape measurements with VLT/SPHERE for ~40 asteroids covering the main compositional classes, thus providing an unprecedented dataset to investigate the origin and collisional evolution of the asteroid belt.

Key words. minor planets, asteroids: individual: (6) Hebe – meteorites, meteors, meteoroids – techniques: high angular resolution

1. Introduction

Disk-resolved imaging is a powerful tool to investigate the origin and collisional history of asteroids. This has been remarkably illustrated by fly-by and rendezvous space missions (Belton et al. 1992, 1996; Zuber et al. 2000; Fujiwara et al. 2006; Sierks et al. 2011; Russell et al. 2012, 2016), as well as observations from the Earth (e.g., Carry et al. 2008, 2010b; Merline et al. 2013). In the late nineties, observations of (4) Vesta with the *Hubble* Space Telescope (HST) led to the discovery of the now-called "Rheasilvia basin" and allowed for establishment of the origin of the Vestoids and HED meteorites found on Earth (Thomas et al. 1997; Binzel et al. 1997). Specifically, it was demonstrated that the basin-forming event on Vesta excavated enough material to account for the family of small asteroids with spectral properties similar to Vesta. HST observations thus confirmed the origin of these bodies as fragments from Vesta, as previously suspected based on spectroscopic measurements (Binzel & Xu 1993). Recently, the Rheasilvia basin was revealed in much greater detail by the Dawn mission, which unveiled two overlapping giant impact features (Schenk et al. 2012).

In the 2000's, a new generation of ground-based imagers with high-angular-resolution capability, such as NIRC2 (Wizinowich et al. 2000; van Dam et al. 2004) on

⋆ Based on observations made with ESO Telescopes at the La Silla Paranal Observatory under programme ID 60.A-9379 and 086.C-0785.

the W. M. Keck II telescope and NACO (Lenzen et al. 2003; Rousset et al. 2003) on the European Southern Observatory (ESO) Very Large Telescope (VLT), made disk-resolved imaging achievable from the ground for a larger number of medium-sized (~100–200-km in diameter) asteroids. In turn, these observations triggered the development of methods for modeling the tridimensional shape of these objects by combining the images with optical light curves (see, e.g., Carry et al. 2010a, 2012; Kaasalainen et al. 2011; Viikinkoski et al. 2015a). These models were subsequently validated by in-situ measurements performed by the ESA Rosetta mission during the fly-by of asteroid (21) Lutetia (Sierks et al. 2011; Carry et al. 2010b, 2012; O'Rourke et al. 2012).

More recently, the newly commissioned VLT/SpectroPolarimetric High-contrast Exoplanet Research instrument (SPHERE) and its very high performance adaptive optics system (Beuzit et al. 2008) demonstrated its ability to reveal in even greater detail the surface of medium-sized asteroids by resolving their largest ($D > 30$ km) craters (Viikinkoski et al. 2015b; Hanuš et al. 2017). This remarkable achievement opens the prospect of a new era of exploration of the asteroid belt and its collisional history.

Here, we use VLT/SPHERE to investigate the shape and topography of asteroid (6) Hebe, a large main-belt asteroid ($D \sim$ 180–200 km; e.g., Tedesco et al. 2004; Masiero et al. 2011) that has long received particular attention from the community of asteroid spectroscopists, meteoricists, and dynamicists. Indeed, Hebe's spectral properties and close proximity to orbital resonances in the asteroid belt make it a possible main source of ordinary H chondrites (i.e., ~34% of the meteorite falls, Hutchison 2004; Farinella et al. 1993; Migliorini et al. 1997; Gaffey & Gilbert 1998; Bottke et al. 2010). It was further proposed that Hebe could be the parent body of an ancient asteroid family (Gaffey & Fieber-Beyer 2013). The idea of H chondrites mainly originating from Hebe, however, was recently weakened by the discovery of a large number of asteroids (including several asteroid families) with similar spectral properties (hence composition, Vernazza et al. 2014). Here, we challenge this hypothesis by studying the three-dimensional shape and topography of Hebe derived from disk-resolved observations. We observed Hebe throughout its rotation in order to derive its shape, and to characterize the largest craters at its surface. When combined with previous adaptive-optics (AO) images and light curves (both from the literature and from recent optical observations by our team), these new observations allow us to derive a reliable shape model and an estimate of Hebe's density based on its astrometric mass (i.e., the mass derived from the study of planetary ephemeris and orbital deflections). Finally, we analyse Hebe's topography by means of an elevation map and discuss the implications for the origin of H chondrites.

2. Observations and data pre-processing

We observed (6) Hebe close to its opposition date while it was orientated "equator-on" (from its spin solution derived below), that is, with an ideal viewing geometry exposing its whole surface as it rotated. Observations were acquired at four different epochs between December 8–12, 2014, such that the variation of the sub-Earth point longitude was 90 ± 30° between each epoch.

Observations were performed with the recently commissioned second-generation SPHERE instrument, mounted at the ESO VLT (Fusco et al. 2006; Beuzit et al. 2008), during the science verification of the instrument[1]. We used IRDIS broad-band classical imaging in Y (filter central wavelength = 1.043 μm, width = 0.140 μm) in the pupil-tracking mode, where the pupil remains fixed while the field orientation varies during the observations, to achieve the best point-spread function (PSF) stability. Each observational sequence consisted in a series of ten images with 2 s exposure time during which Hebe was used as a natural guide star for AO corrections. Observations were performed under average seeing conditions (0.9–1.1″) and clear sky transparency, at an airmass of ~1.1.

Sky backgrounds were acquired along our observations for data-reduction purposes. At the end of each sequence, we observed the nearby star HD 26086 under the exact same AO configuration as the asteroid to estimate the instrument PSF for deconvolution purposes. Finally, standard calibrations, which include detector flat-fields and darks, were acquired in the morning as part of the instrument calibration plan.

Data pre-processing of the IRDIS data made use of the preliminary release (v0.14.0-2) of the SPHERE data reduction and handling (DRH) software (Pavlov et al. 2008), as well as additional tools written in the interactive data language (IDL), in order to perform background subtraction, flat-fielding and bad-pixel correction. The pre-processed images were then aligned one with respect to the others using the IDL ML_SHIFTFINDER maximum likelihood function, and averaged to maximise the signal to noise ratio of the asteroid. Finally, the optimal angular resolution of each image ($\lambda/D = 0.026''$, corresponding to a projected distance of 22 km) was restored with Mistral, a myopic deconvolution algorithm optimised for images with sharp boundaries (Fusco et al. 2002; Mugnier et al. 2004), using the stellar PSF acquired on the same night as our asteroid data.

3. Additional data

3.1. Disk-resolved images

To reconstruct the 3D shape of (6) Hebe, we compiled available images obtained with the earlier-generation AO instruments NIRC2 (Wizinowich et al. 2000; van Dam et al. 2004) on the W. M. Keck II telescope and NACO (Lenzen et al. 2003; Rousset et al. 2003) on the ESO VLT. Each of these images, as well as the corresponding calibration files and stellar PSF, were retrieved from the Canadian Astronomy Data Center[2] (Gwyn et al. 2012) or directly from the observatory's database. Data processing and Mistral deconvolution of these images were performed following the same method as for our SPHERE images. Only a subset of the 25 different epochs listed in Table 1 had been published (Hanuš et al. 2013).

3.2. Optical light curves

We used 38 light curves obtained in the years 1953–1993 and available in the Database of Asteroid Models from Inversion Techniques (DAMIT[3], Durech et al. 2010) that were used by Torppa et al. (2003) to derive the pole orientation and convex shape of (6) Hebe from light curve inversion (Kaasalainen & Torppa 2001; Kaasalainen 2001). We also retrieved 16 light curves observed by the amateurs F. Kugel

[1] Observations obtained under ESO programme ID 60.A-9379 (P.I. C. Dumas).
[2] http://www.cadc-ccda.hia-iha.nrc-cnrc.gc.ca/
[3] http://astro.troja.mff.cuni.cz/projects/asteroids3D

Table 1. Date, mid-observing time (UTC), heliocentric distance (Δ) and range to observer (r), phase angle (α), apparent size (Θ), longitude (λ) and latitude (β) of the subsolar and subobserver points (SSP, SEP).

	Date	UTC	Instrument	Δ (AU)	r (AU)	α (°)	Θ ($''$)	SEP_λ (°)	SEP_β (°)	SSP_λ (°)	SSP_β (°)
1	2002-05-07	14:08:54	Keck/NIRC2[1]	2.52	1.88	20.5	0.131	66.1	–34.4	53.3	–17.4
2	2002-05-08	13:55:01	Keck/NIRC2[1]	2.52	1.86	20.4	0.119	329.8	–34.5	317.2	–17.5
3	2002-09-27	06:29:51	Keck/NIRC2[2]	2.21	1.91	27.0	0.098	162.5	–19.4	187.2	–35.4
4	2007-12-15	14:15:39	Keck/NIRC2[3]	2.47	1.86	20.8	0.149	14.2	32.9	356.2	19.6
5	2007-12-15	14:30:31	Keck/NIRC2[3]	2.47	1.86	20.8	0.145	1.9	32.9	343.9	19.6
6	2007-12-15	14:44:49	Keck/NIRC2[3]	2.47	1.86	20.8	0.145	350.1	32.9	332.1	19.6
7	2007-12-15	15:00:54	Keck/NIRC2[3]	2.47	1.86	20.8	0.138	336.8	32.9	318.9	19.6
8	2007-12-15	15:27:39	Keck/NIRC2[3]	2.47	1.86	20.8	0.143	314.8	32.9	296.8	19.6
9	2007-12-15	16:26:58	Keck/NIRC2[3]	2.47	1.86	20.8	0.151	265.9	32.9	247.9	19.6
10	2009-06-07	10:52:24	Keck/NIRC2[2]	2.81	2.01	15.1	0.129	43.1	8.0	57.9	4.9
11	2010-06-28	13:08:00	Keck/NIRC2[4]	2.06	1.62	28.9	0.168	258.8	–39.3	221.2	–39.0
12	2010-08-26	12:47:10	Keck/NIRC2[3]	1.98	1.05	16.1	0.260	48.5	–27.4	30.6	–31.2
13	2010-08-26	13:04:26	Keck/NIRC2[3]	1.98	1.05	16.1	0.260	34.3	–27.4	16.3	–31.2
14	2010-08-26	13:59:47	Keck/NIRC2[3]	1.98	1.05	16.1	0.265	348.6	–27.4	330.7	–31.2
15	2010-08-26	14:38:00	Keck/NIRC2[3]	1.98	1.05	16.1	0.270	317.1	–27.4	299.2	–31.2
16	2010-11-29	07:10:28	Keck/NIRC2[4]	1.94	1.39	28.9	0.189	160.9	–22.9	191.5	–18.5
17	2010-12-13	01:18:16	VLT/NACO[5]	1.94	1.52	30.0	0.153	28.9	–23.2	59.6	–15.3
18	2010-12-13	02:40:24	VLT/NACO[5]	1.94	1.53	30.0	0.171	321.1	–23.2	351.8	–15.3
19	2010-12-14	00:41:59	VLT/NACO[5]	1.94	1.53	30.0	0.171	311.5	–23.2	342.2	–15.1
20	2010-12-14	01:38:22	VLT/NACO[5]	1.94	1.54	30.0	0.158	265.0	–23.2	295.7	–15.1
21	2010-12-14	02:14:10	VLT/NACO[5]	1.94	1.54	30.0	0.167	235.5	–23.2	266.2	–15.0
22	2014-12-08	00:53:28	VLT/SPHERE[6]	2.03	1.15	17.0	0.216	208.7	3.4	225.7	2.8
23	2014-12-09	01:04:54	VLT/SPHERE[6]	2.03	1.16	17.2	0.211	91.6	3.2	108.9	3.0
24	2014-12-10	01:59:38	VLT/SPHERE[6]	2.03	1.17	17.5	0.221	298.8	3.0	316.4	3.2
25	2014-12-12	04:14:08	VLT/SPHERE[6]	2.04	1.18	18.1	0.221	332.6	2.6	350.7	3.7

Notes. PIs of these observations were [(1)] J.-L. Margot; [(2)] W. J. Merline; [(3)] W. M. Keck engineering team; [(4)] F. Marchis; [(5)] B. Carry; and [(6)] C. Dumas.

and J. Caron, from the *Courbe de Rotation group*[4], and 84 light curves from the data archive of the SuperWASP survey (Pollacco et al. 2006) for the period 2006–2009. This survey aims at finding and characterizing exoplanets by observation of their transit in front of their host star. Its large field of view and cadence provides a goldmine for asteroid light curves (Grice et al. 2017). Finally, four light curves were acquired by our group during April 2016 with the 60 cm TRAPPIST telescope (Jehin et al. 2011).

3.3. Stellar occultations

We retrieved the five stellar occultations listed by Dunham et al. (2016) and publicly available on the Planetary Data System (PDS)[5] for (6) Hebe. We convert the disappearance and reappearance timings of the occulted stars into segments (called chords) on the plane of the sky, using the location of the observers on Earth and the apparent motion of Hebe following the recipes by Berthier (1999). Of the five events, only two had more than one positive chord (that is a recorded blink event) and could be used to constrain the 3D shape (1977-03-05 – also presented in Taylor & Dunham 1978 – and 2008-02-20).

[4] http://obswww.unige.ch/~behrend/page_cou.html
[5] http://sbn.psi.edu/pds/resource/occ.html

3.4. Mid-infrared thermal measurements

Finally, we compiled available mid-infrared thermal measurements to 1) validate, independently of the AO images, the size of our 3D-shape model and; 2) derive the thermal properties of the surface of Hebe through thermophysical modeling of the infrared flux. Specifically, we used a total of 103 thermal data points from IRAS (12, 25, 60, 100 μm, Tedesco et al. 2002), AKARI-IRC (9, 18 μm, Usui et al. 2011), ISO-ISOPHOT (25 μm, Lagerros et al. 1999), and *Herschel*-PACS (70, 100, 160 μm, Müller et al., in prep.).

4. 3D shape, volume, and density

Recent algorithms such as KOALA (Carry et al. 2010a, 2012; Kaasalainen et al. 2011) and ADAM (Viikinkoski et al. 2015a) allow simultaneous derivation of the spin, 3D shape, and size of an asteroid (see, e.g., Merline et al. 2013; Tanga et al. 2015; Viikinkoski et al. 2015b; Hanuš et al. 2017). This combined multi-data approach has been validated by comparing the 3D shape model of (21) Lutetia by Carry et al. (2010b) with the images returned by the ESA Rosetta mission during its fly-by of the asteroid (see Sierks et al. 2011; Carry et al. 2012).

Here, we reconstruct the spin and shape of (6) Hebe with ADAM, which iteratively improves the solution by minimizing the residuals between the Fourier transformed images and a projected polyhedral model. This method allows the use of AO images directly without requiring the extraction of boundary contours. Boundary contours are therefore used here only as a means

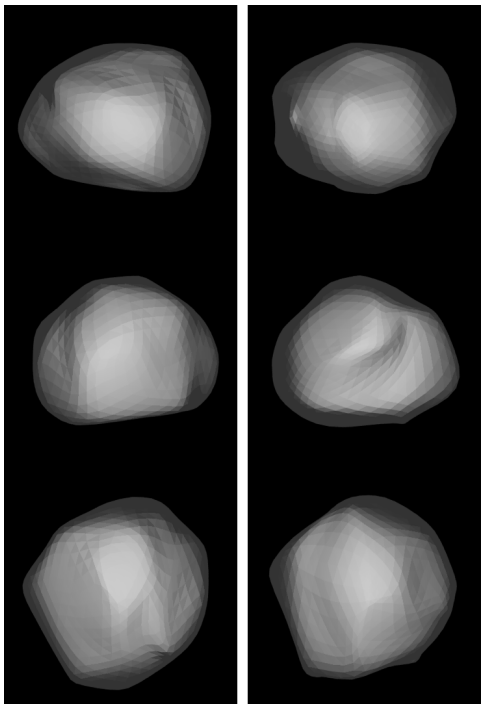

Fig. 1. 3D-shape model of (6) Hebe reconstructed from light curves and all resolved images (*left*), and from light curves and SPHERE images only (*right*). Viewing directions are two equator-on views rotated by 90° and a pole-on view.

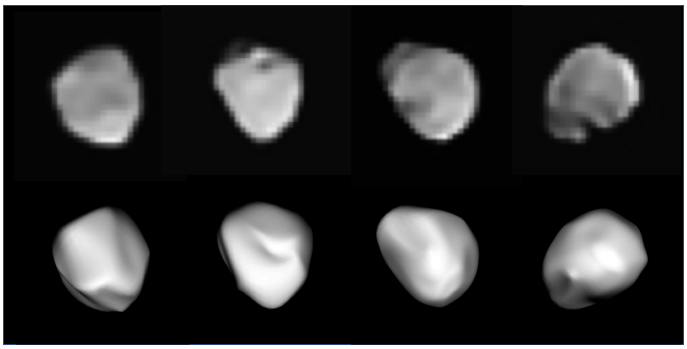

Fig. 2. Deconvolved SPHERE images of Hebe obtained between 8 and 12 December 2014 (top) and corresponding projection of the model (bottom). Orientation of the four images with respect to the north is 15.2°, 12.8°, –5.3° and –89.6° , respectively.

Table 2. Period, spin (ECJ2000 longitude λ, latitude β and initial Julian date T_0), and dimensions (volume-equivalent diameter D, volume V, and tri-axial ellipsoid diameters a, b, c along principal axes of inertia) of Hebe derived with ADAM.

Parameter	Value (all AO)	Value (SPHERE-only)	Unc.	Unit
Period	7.274467	7.274465	5×10^{-5}	hour
λ	341.7	343.2	3	deg.
β	+49.9	+46.8	4	deg.
T_0	2434569.00	2434569.00		
D	196	193	6	km
V	3.95×10^6	3.75×10^6	1.2×10^5	km^3
a	218.4	213.4	6.0	km
b	206.2	200.2	6.0	km
c	172.1	172.6	6.0	km
a/b	1.06	1.07	0.04	
b/c	1.20	1.16	0.05	

to measure the pixel root mean square (RMS) residuals between the location of the asteroid silhouette on the observed and modeled images. ADAM offers two different shape supports: subdivision surfaces and octanoids based on spherical harmonics. Here, we use the subdivision surfaces parametrisation which offers more local control on the model than global representations (see Viikinkoski et al. 2015a).

Two different models depicted in Fig. 1 were obtained; the first one using the light curves combined to the full AO sample, and the second one using the light curves and the SPHERE images only. Comparison of the SPHERE-based model with our SPHERE images, earlier AO images, subsets of optical light curves and stellar occultations are presented in Figs. 2–5, respectively.

The two models nicely fit all data, the RMS residuals between the observations and the predictions by the model being only 0.6 pixels for the location of the asteroid contours, 0.02 mag for the light curves, and 5 km for the stellar occultation of 2008 (the occultation of 1977 has very large uncertainties on its timings). The 3D shape models are close to an oblate spheroid, and have a volume-equivalent diameter of 196 ± 6 km (all AO) and 193 ± 6 km (SPHERE-based; Table 2). Spin-vector coordinates (λ, β in ECJ2000) are close to earlier estimates based on light-curve inversion ((339°, +45°), Torppa et al. 2003) and on a combination of light curves and AO images ((345°, +42°), Hanuš et al. 2013).

The main difference between the two shape models comes from the presence of some surface features in the SPHERE-based model that are lacking in the model obtained using the full dataset of AO images. This is due to the lower resolution of earlier AO images that do not address some of the small-scale surface features revealed by the SPHERE images.

There are 12 diameter estimates for Hebe in the literature (Table A.1, Fig. A.1). Rejecting values that do not fall within one standard deviation of the average value of the full dataset gives an average equivalent-volume sphere diameter of 191.5 ± 8.3 km, in very good agreement with the values of 193±6 km and 196 ± 6 km derived here (also supported by the thermophysical analysis presented in the following section). In the following, we use the value of the diameter obtained from our SPHERE-based model, which is more precise due to the higher angular resolution of the SPHERE images with respect to the NIRC2 and NACO images. A main advantage of using a diameter obtained from a full 3D shape modeling resides in the uncertainty on the derived volume V, which is close to $\delta V/V \approx \delta D/D$, as opposed to a $\delta V/V \approx 3\delta D/D$ in the spherical assumption used in most aforementioned estimates (see Kaasalainen & Viikinkoski 2012 for details).

Combining this diameter with an average mass of 1.31 ± 0.24 × 10^{19} kg computed from 16 estimates gathered from the literature (Table A.2, Fig. A.2), provides a bulk density of 3.48 ± 0.64 g cm^{-3}, in perfect agreement with the average grain density of ordinary H chondrites (3.42±0.18 g cm^{-3}; Consolmagno et al. 2008). The derived density therefore suggests a null internal porosity, consistent with an intact internal structure. Hebe hence appears to reside in the volumetric and structural transitional region between the compact and gravity-shaped dwarf planets, and the medium-sized asteroids (~10–100 km in diameter) with fractured interior (Carry 2012; Scheeres et al. 2015). However,

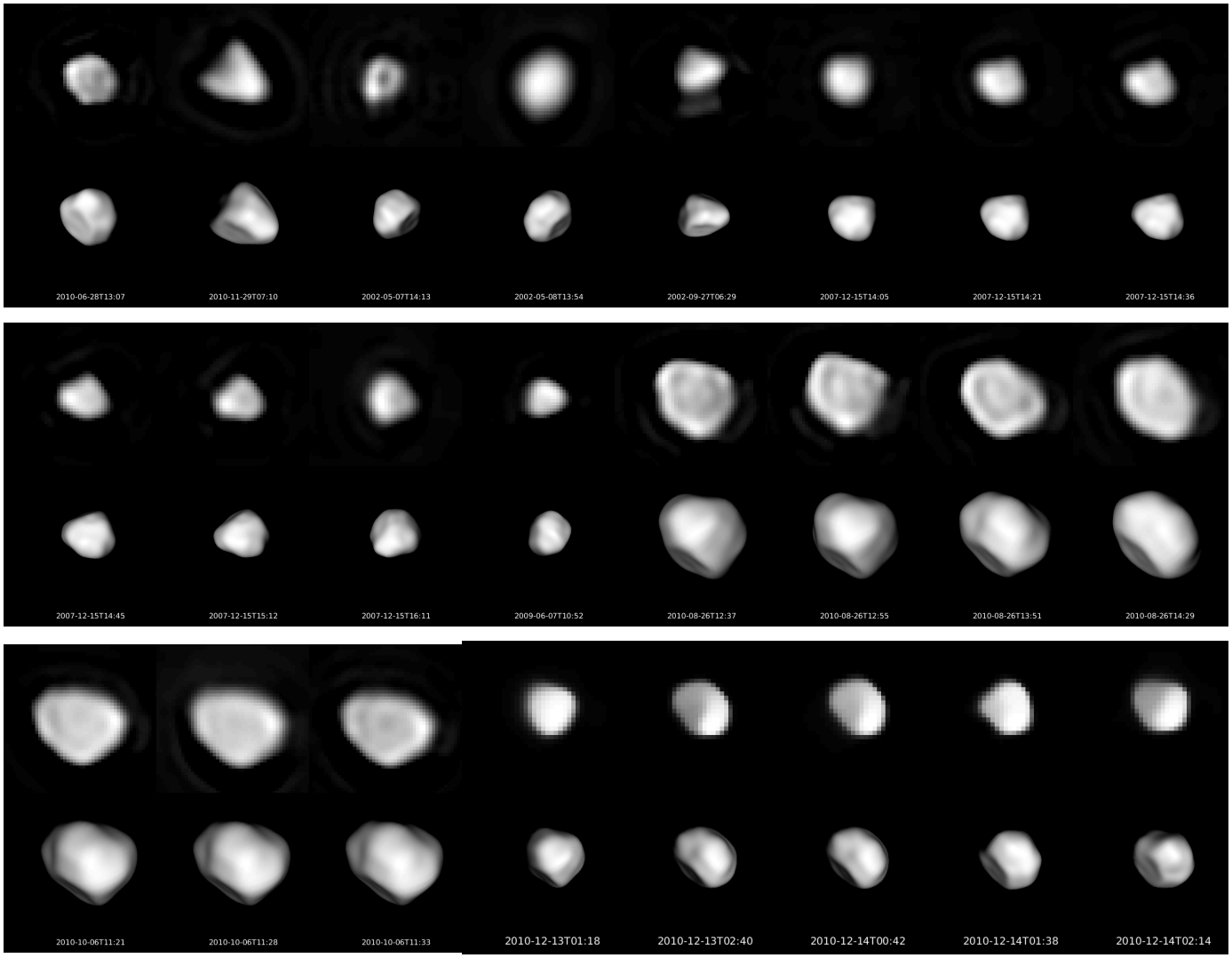

Fig. 3. Previous AO images of Hebe obtained with Keck/NIRC2 and VLT/NACO (*top of the three rows*) and corresponding projection of the model (*bottom*). Each image is 0.8″ × 0.8″ in size.

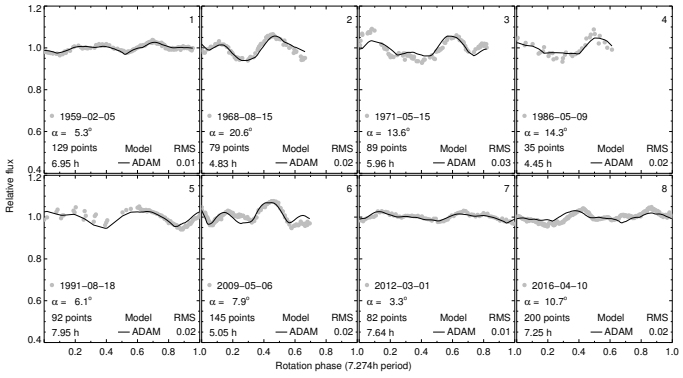

Fig. 4. Comparison of the synthetic light curves (solid line) from the shape model with a selection of light curves (gray points).

due to the current large mass uncertainty that dominates the uncertainty of the bulk density, the possibility of higher internal porosity cannot be ruled out. We expect the *Gaia* mission to trigger higher-precision mass estimates in the near future (Mignard et al. 2007; Mouret et al. 2007) that will help refine the density measurement of Hebe.

5. Thermal parameters and regolith grain size

A thermophysical model (TPM; Müller & Lagerros 1998; Müller et al. 1999) was also used to provide an independent size measurement for Hebe and to derive its thermal surface properties. The TPM uses as input our 3D shape model with unscaled diameter. The procedure is described in detail in Appendix B.

Using absolute magnitude $H = 5.71$ and magnitude slope $G = 0.27$ from the Asteroid Photometric Catalogue (Lagerkvist & Magnusson 2011), the TPM provides a solution for diameter and albedo of (D, p_v) = (198^{+4}_{-2} km, 0.24 ± 0.01), in good agreement with the size of our 3D-shape model and previous albedo measurements from IRAS ($p_v = 0.27 \pm 0.01$; Tedesco et al. 2002), WISE ($p_v = 0.24 \pm 0.04$; Masiero et al. 2014) and AKARI ($p_v = 0.24 \pm 0.01$; Usui et al. 2011). Best-fitting solutions are found for significant surface roughness (in agreement with Lagerros et al. 1999), and thermal inertia Γ values ranging from 15 to 90 J m^{-2} s$^{-0.5}$ K^{-1}, with a preference for $\Gamma \approx 50$ J m^{-2} s$^{-0.5}$ K^{-1}. Interestingly, we note that the best-fitting solution for Γ drops from ∼60 J m^{-2} s$^{-0.5}$ K^{-1} when only considering thermal measurements acquired at $r < 2.1$ AU, to ∼40 J m^{-2} s$^{-0.5}$ K^{-1} for data taken at $r > 2.6$ AU. While this might be indicative of changing thermal inertia with

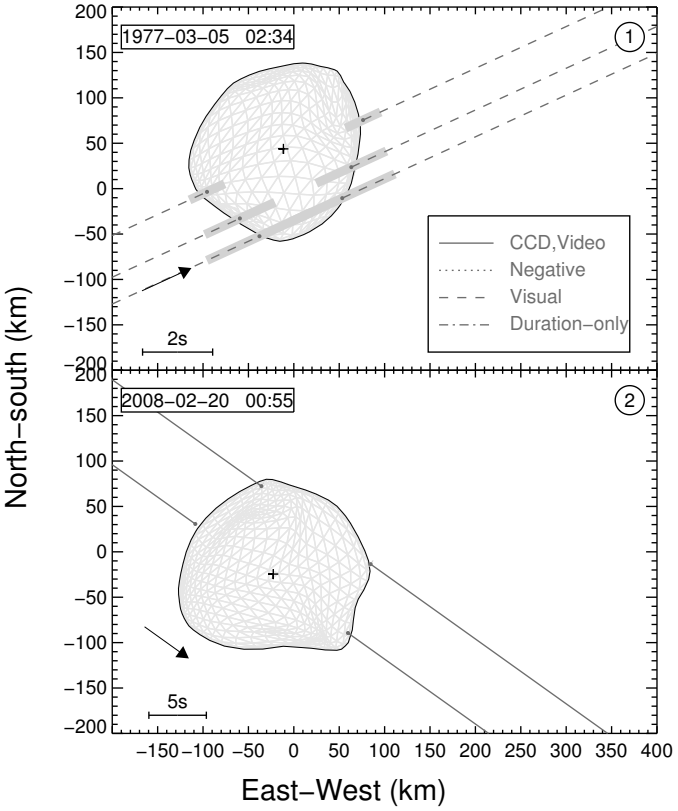

Fig. 5. Comparison of the shape model with the chords from the occultation of 1977 and 2008.

temperature, this result should be taken with extreme caution, as the TPM probably overfits the data due to the large error bars on the thermal measurements (see Appendix B).

From the thermal inertia value derived here, one can further derive the grain size of the surface regolith of Hebe (Gundlach & Blum 2013). Assuming values of heat capacity and material density typical of H5 ordinary chondrites (Opeil et al. 2010) and estimated surface temperature of 230 K and 180 K at 1.94 and 2.87 AU respectively, we find that the typical grain size of Hebe is about 0.2–0.3 mm (see Annexe B for more details).

6. Topography

Hebe's topography was investigated by generating an elevation map of its surface with respect to a volume-equivalent ellipsoid best-fitting our 3D-shape model, following the method by Thomas (1999). This map shown in Figure 6 allows the identification of several low-topographic and concave regions possibly created by impacts (the two shape models depicted in Fig. 1 produce slightly different but consistent topographic maps). Specifically, five large depressions (numbered 1 to 5 on the elevation map) are found at the surface of Hebe, at (29°, 43°), (93°, –42°), (190°, 35°), (289°, –13°), and near the south pole. Estimated dimensions (diameter D and maximum depth below the average surface d) are D_1 = 92–105 km, d_1 = 13 km; D_2 = 85–117 km, d_2 = 12 km; D_3 = 68–83 km, d_3 = 11 km; D_4 = 75–127 km, d_4 = 18 km; and D_5 = 42–52 km, d_5 = 7 km, respectively.

Assuming that the volume of a crater relates approximately to the volume of ejecta produced by the impact – which is most likely very optimistic because 1) a significant fraction of impact crater volume comes from compression (Melosh 1989) and; 2) at least a fraction of the ejecta must have re-accumulated on the surface of the body (e.g., Marchi et al. 2015), one can further estimate the volume of a hypothetical family derived from an impact on Hebe. The largest depression on Hebe roughly accounts for a volume of 10^5 km^3, corresponding to a body with an equivalent diameter of ~58 km.

For comparison, the five known S-type families spectrally analogous to Hebe (therefore to H chondrites; Vernazza et al. 2014) and located close to the main-belt 3:1 and 5:2 mean-motion resonances, namely Agnia (located at semi-major axis a = 2.78 AU and eccentricity e = 0.09), Koronis (a = 2.87 AU, e = 0.05), Maria (a = 2.55 AU, e = 0.06), Massalia (a = 2.41 AU, e = 0.14) and Merxia (a = 2.75 AU, e = 0.13) encompass a total volume of respectively ~2.4×10^4 km^3, 5.6×10^5 km^3, 3.6×10^5 km^3, 5.7×10^4 km^3 and 1.8×10^4 km^3 when the larger member of each family is removed. Family membership was determined using Nesvorný (2015)'s hierarchical clustering method (HCM)-based classification[6] and rejecting possible interlopers that do not fit the "V-shape" criterion as defined in Nesvorný et al. (2015). The diameter of each asteroid identified as a family member was retrieved from the WISE/NEOWISE database (Masiero et al. 2011) when available, or estimated from its absolute H magnitude otherwise, assuming an albedo equal to that of the largest member of its family (respectively 0.152, 0.213, 0.282, 0.241 and 0.213 for (847) Agnia, (158) Koronis, (170) Maria, (20) Massalia and (808) Merxia; https://mp3c.oca.eu). We note that these values should be considered as lower limits as those families certainly include smaller members beyond the detection limit.

We therefore find that the volume of material corresponding to the largest depression on Hebe is of the order of some H-chondrite-like S-type families, and ~4–6 times smaller than the largest ones. Therefore, although we cannot firmly exclude Hebe as the main (or unique) source of H chondrites, it appears that such a hypothesis is not the most likely one. This is further strengthened by the following two arguments. First, it seems improbable that the volume excavated from Hebe's largest depression, which we find to be roughly 10 to 30 times smaller than the volume of the Rheasilvia basin on Vesta (Schenk et al. 2012), would contribute to ~34% of the meteorite falls, when HED meteorites only represent ~6% of the falls (Hutchison 2004). We note, however, that the low number of HED meteorites may also relate to the relatively old age (Schenk et al. 2012) of the Vesta family (Heck et al. 2017). Second, the current lack of observational evidence for a Hebe-derived family indicates that such a family, if it ever existed, must be very ancient and dispersed. Yet, there is growing evidence from laboratory experiments that the current meteorite flux must be dominated by fragments from recent asteroid breakups (Heck et al. 2017). In the case of H chondrites, this is well supported by their cosmic ray exposure ages (Marti & Graf 1992; Eugster et al. 2006). It therefore appears that a recent – yet to be identified – collision suffered by another H-chondrite-like asteroid is the most likely source of the vast majority of H chondrites.

7. Conclusion and outlook

We have reconstructed the spin and tridimensional shape of (6) Hebe from combined AO images and optical light curves, and checked the consistency of the derived model against available stellar occultations and thermal measurements. Whereas the irregular shape of Hebe suggests it was moulded by impacts, its density appears indicative of a compact interior. Hebe thus

[6] http://sbn.psi.edu/pds/resource/nesvornyfam.html

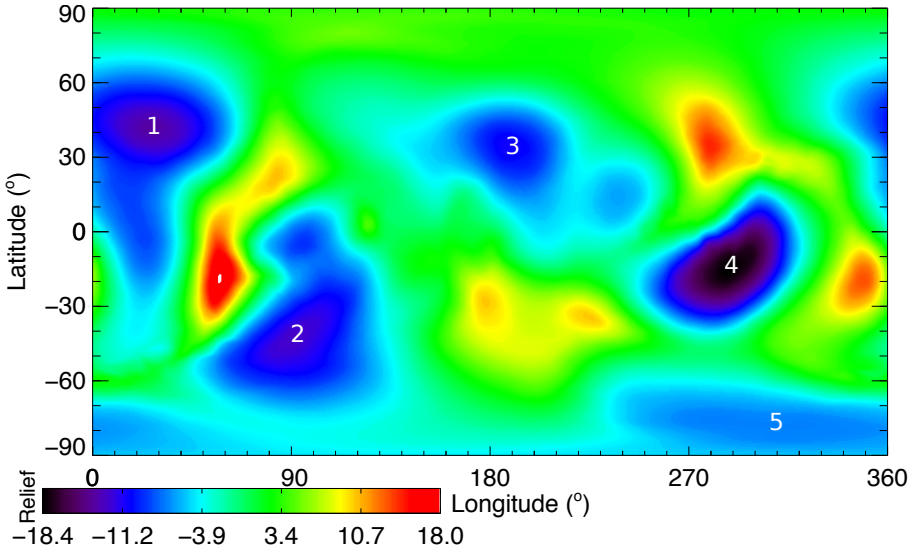

Fig. 6. Elevation map (in km) of (6) Hebe, with respect to a volume-equivalent ellipsoid best fitting our 3D-shape model. The five major depressions are identified by numbers.

seems to reside in the structural regime in transition between round-shaped dwarf planets shaped by gravity, and medium-sized asteroids with fractured interiors (i.e., significant fractions of macro-porosity; Carry 2012). This however needs to be confirmed by future mass measurements (e.g., from *Gaia* high-precision astrometric measurements) that will help improve the current mass uncertainty that dominates the uncertainty on density.

The high angular resolution of SPHERE further allowed us to identify several concave regions at the surface of Hebe possibly indicative of impact craters. We find the volume of the largest depression to be roughly five times smaller than the volume of the largest S-type H-chondrite-like families located close to orbital resonances in the asteroid belt. Furthermore, this volume is more than an order of magnitude smaller than the volume of the Rheasilvia basin on Vesta (Schenk et al. 2012) from which HED meteorites (∼6% of the falls) originate. Our results therefore imply that (6) Hebe is not the most likely source of ordinary H chondrites (∼34% of the falls).

Finally, this work has demonstrated the potential of SPHERE to bring important constraints on the origin and collisional history of the main asteroid belt. Over the next two years, our team will collect – via a large program on VLT/SPHERE (run ID: 199.C-0074, PI: Pierre Vernazza) – similar volume, shape, and topographic measurements for a significant number (∼40) of $D \geq 100$ km asteroids sampling the four major compositional classes (S, Ch/Cgh, B/C and P/D).

Acknowledgements. Based on observations made with ESO Telescopes at the La Silla Paranal Observatory under programme ID 60.A-9379. The asteroid diameters and albedos based on NEOWISE observations were obtained from the Planetary Data System (PDS). Some of the data presented herein were obtained at the W.M. Keck Observatory, which is operated as a scientific partnership among the California Institute of Technology, the University of California and the National Aeronautics and Space Administration. The Observatory was made possible by the generous financial support of the W.M. Keck Foundation. This research has made use of the Keck Observatory Archive (KOA), which is operated by the W. M. Keck Observatory and the NASA Exoplanet Science Institute (NExScI), under contract with the National Aeronautics and Space Administration. The authors wish to recognize and acknowledge the very significant cultural role and reverence that the summit of Mauna Kea has always had within the indigenous Hawaiian community. We are most fortunate to have the opportunity to conduct observations from this mountain. This research used the MP^{3}C service developed, maintained, and hosted at the Lagrange laboratory, Observatoire de la Côte d'Azur (Delbo et al. 2017). Photometry of 6 Hebe was identified and extracted from WASP data with the help of Neil Parley (Open University, now IEA Reading). The WASP project is currently funded and operated by Warwick University and Keele University, and was originally set up by Queen's University Belfast, the Universities of Keele, St. Andrews and Leicester, the Open University, the Isaac Newton Group, the Instituto de Astrofisica de Canarias, the South African Astronomical Observatory and by STFC. The WASP project is currently funded and operated by Warwick University and Keele University, and was originally set up by Queen's University Belfast, the Universities of Keele, St. Andrews and Leicester, the Open University, the Isaac Newton Group, the Instituto de Astrofisica de Canarias, the South African Astronomical Observatory and by STFC. TRAPPIST-South is a project funded by the Belgian Funds (National) de la Recherche Scientifique (F.R.S.-FNRS) under grant FRFC 2.5.594.09.F, with the participation of the Swiss National Science Foundation (FNS/SNSF). E.J. and M.G. are F.R.S.-FNRS research associates. Based on observations with ISO, an ESA project with instruments funded by ESA Member States and with the participation of ISAS and NASA. *Herschel* is an ESA space observatory with science instruments provided by European-led Principal Investigator consortia and with important participation from NASA. *Herschel* fluxes of Hebe where extracted by Csaba Kiss (Konkoly Observatory, Research Centre for Astronomy and Earth Sciences, Hungarian Academy of Sciences, H-1121 Budapest, Konkoly Thege Miklós út 15–17, Hungary). TM received funding from the European Union's Horizon 2020 Research and Innovation Programme, under Grant Agreement No. 687378.

References

Baer, J., & Chesley, S. R. 2008, Celest. Mech. Dyn. Astron., 100, 27
Baer, J., Chesley, S. R., & Matson, R. D. 2011, AJ, 141, 143
Belton, M. J. S., Veverka, J., Thomas, P., et al. 1992, Science, 257, 1647
Belton, M. J. S., Chapman, C. R., Klaasen, K. P., et al. 1996, Icarus, 120, 1
Berthier, J. 1999, Notes scientifiques et techniques du Bureau des longitudes, S064
Beuzit, J.-L., Feldt, M., Dohlen, K., et al. 2008, Ground-based and Airborne Instrumentation for Astronomy II, Proc. SPIE, 7014, 701418
Binzel, R. P., & Xu, S. 1993, Science, 260, 186
Binzel, R. P., Gaffey, M. J., Thomas, P. C., et al. 1997, Icarus, 128, 95
Bottke, W., Vokrouhlický, D., Nesvorný, D., & Shrbeny, L. 2010, BAAS, 42, 1051
Carry, B. 2012, Planet. Space Sci., 73, 98
Carry, B., Dumas, C., Fulchignoni, M., et al. 2008, A&A, 478, 235
Carry, B., Dumas, C., Kaasalainen, M., et al. 2010a, Icarus, 205, 460
Carry, B., Kaasalainen, M., Leyrat, C., et al. 2010b, A&A, 523, A94
Carry, B., Kaasalainen, M., Merline, W. J., et al. 2012, Planet. Space Sci., 66, 200
Consolmagno, G., Britt, D., & Macke, R. 2008, Chemie der Erde/Geochemistry, 68, 1

Delbo, M., Tanga, P., Carry, B., Ordenovic, C., & Bottein, P. 2017, The minor planet physical properties catalogue, Int. Conf. Asteroids, Comets, and Meteors: ACM 2017
Dunham, D. W., & Mallen, G. 1979, Rev. Mex. Astron. Astrofis., 4, 205
Dunham, D. W., Herald, D., Frappa, E., et al. 2016, NASA Planetary Data System, 243
Durech, J., Sidorin, V., & Kaasalainen, M. 2010, A&A, 513, A46
Durech, J., Kaasalainen, M., Herald, D., et al. 2011, Icarus, 214, 652
Eugster, O., Herzog, G. F., Marti, K., & Caffee, M. W. 2006, in Meteorites and the Early Solar System II (Tucson: University of Arizona Press), 829
Farinella, P., Gonczi, R., Froeschle, C., & Froeschlé, C. 1993, Icarus, 101, 174
Fienga, A., Laskar, J., Morley, T., et al. 2009, A&A, 507, 1675
Fienga, A., Laskar, J., Kuchynka, P., et al. 2011, Celest. Mech. Dyn. Astron., 111, 363
Fienga, A., Manche, H., Laskar, J., Gastineau, M., & Verma, A. 2013, ArXiv e-prints [arXiv:1301.1510]
Fienga, A., Manche, H., Laskar, J., Gastineau, M., & Verma, A. 2014, ArXiv e-prints [arXiv:1405.0484]
Folkner, W. M., Williams, J. G., & Boggs, D. H. 2009, Interplanetary Network Progress Report, 178, 1
Fujiwara, A., Kawaguchi, J., Yeomans, D. K., et al. 2006, Science, 312, 1330
Fusco, T., Mugnier, L. M., Conan, J.-M., et al. 2002, in Astronomical Telescopes and Instrumentation, eds. P. L. Wizinowich, & D. Bonaccini (SPIE), 1065
Fusco, T., Rousset, G., Sauvage, J. F., et al. 2006, Optics Express, 14, 7515
Gaffey, M. J., & Fieber-Beyer, S. K. 2013, Meteor. Planet. Sci. Suppl., 76
Gaffey, M. J., & Gilbert, S. L. 1998, Meteor. Planet. Sci., 33, 1281
Goffin, E. 2014, A&A, 565, A56
Grice, J., Snodgrass, C., Green, S., Parley, N., & Carry, B. 2017, The shapes of primordial asteroids, Int. Conf. Asteroids, Comets, and Meteors: ACM 2017
Gundlach, B., & Blum, J. 2013, Icarus, 223, 479
Gwyn, S. D. J., Hill, N., & Kavelaars, J. J. 2012, PASP, 124, 579
Hanuš, J., Marchis, F., & Durech, J. 2013, Icarus, 226, 1045
Hanuš, J., Marchis, F., Viikinkoski, M., Yang, B., & Kaasalainen, M. 2017, A&A, 599, A36
Heck, P. R., Schmitz, B., Bottke, W. F., et al. 2017, Nat. Astron., 1, 0035
Hutchison, R. 2004, Meteorites, Cambridge Planetary Science (Cambridge University Press)
Jehin, E., Gillon, M., Queloz, D., et al. 2011, The Messenger, 145, 2
Kaasalainen, M. 2001, Icarus, 153, 37
Kaasalainen, M., & Torppa, J. 2001, Icarus, 153, 24
Kaasalainen, M., & Viikinkoski, M. 2012, A&A, 543, A97
Kaasalainen, M., Viikinkoski, M., Carry, B., et al. 2011, EPSC-DPS Joint Meeting 2011, 416
Kochetova, O. M. 2004, Sol. Syst. Res., 38, 66
Kochetova, O. M., & Chernetenko, Y. A. 2014, Sol. Syst. Res., 48, 295
Konopliv, A. S., Asmar, S. W., Folkner, W. M., et al. 2011, Icarus, 211, 401
Kuchynka, P., & Folkner, W. M. 2013, Icarus, 222, 243
Lagerkvist, C. I., & Magnusson, P. 2011, NASA Planetary Data System, 162
Lagerros, J. S. V., Müller, T. G., Klaas, U., & Erikson, A. 1999, Icarus, 142, 454
Lenzen, R., Hartung, M., Brandner, W., et al. 2003, Instrument design and Performance for optical/Infrared Ground-based Telescopes, Proc. SPIE, 4841, 944
Marchi, S., Chapman, C. R., Barnouin, O. S., Richardson, J. E., & Vincent, J. B. 2015, in Asteroids IV (University of Arizona Press)
Marti, K., & Graf, T. 1992, Ann. Rev. Earth Planet. Sci., 20, 221
Masiero, J. R., Mainzer, A. K., Grav, T., et al. 2011, ApJ, 741, 68
Masiero, J. R., Grav, T., Mainzer, A. K., et al. 2014, ApJ, 791, 121
Melosh, H. J. 1989, Oxford Monographs on Geology and Geophysics (Oxford University Press), 11
Merline, W. J., Drummond, J. D., Carry, B., et al. 2013, Icarus, 225, 794
Michalak, G. 2001, A&A, 374, 703
Migliorini, F., Manara, A., Scaltriti, F., et al. 1997, Icarus, 128, 104
Mignard, F., Cellino, A., Muinonen, K., et al. 2007, Earth Moon Planets, 101, 97
Morrison, D. 1974, ApJ, 194, 203
Morrison, D. 1977, Icarus, 31, 185
Mouret, S., Hestroffer, D., & Mignard, F. 2007, A&A, 472, 1017
Mugnier, L. M., Fusco, T., & Conan, J.-M. 2004, J. Opt. Soc. Am. A, 21, 1841
Müller, T. G., & Lagerros, J. S. V. 1998, A&A, 338, 340
Müller, T. G., Lagerros, J. S. V., Burgdorf, M., et al. 1999, Asteroids, Comets, and Meteors: ACM 2002, 427, 141
Nesvorný, D. 2015, NASA Planetary Data System, 234
Nesvorný, D., Brož, M., & Carruba, V. 2015, in Asteroids IV, eds. P. Michel et al., 297
Opeil, C. P., Consolmagno, G. J., & Britt, D. T. 2010, Icarus, 208, 449
O'Rourke, L., Müller, T., Valtchanov, I., et al. 2012, Planet. Space Sci., 66, 192
Pavlov, A., Möller-Nilsson, O., Feldt, M., et al. 2008, in Advanced Software and Control for Astronomy II, Proc. SPIE, 7019, 701939
Pitjeva, E. V. 2013, Sol. Syst. Res., 47, 386
Pollacco, D. L., Skillen, I., Collier Cameron, A., et al. 2006, PASP, 118, 1407
Rousset, G., Lacombe, F., Puget, P., et al. 2003, Adaptive optical system Technologies II, Proc. SPIE, 4839, 140
Russell, C. T., Raymond, C. A., Coradini, A., et al. 2012, Science, 336, 684
Russell, C. T., Raymond, C. A., Ammannito, E., et al. 2016, Science, 353, 1008
Ryan, E. L., & Woodward, C. E. 2010, AJ, 140, 933
Scheeres, D. J., Britt, D., Carry, B., & Holsapple, K. A. 2015, in Asteroid Interiors and Morphology, eds. P. Michel, F. E. DeMeo, & W. F. Bottke (University of Arizona Press), 745
Schenk, P., O'Brien, D. P., Marchi, S., et al. 2012, Science, 336, 694
Sierks, H., Lamy, P., Barbieri, C., et al. 2011, Science, 334, 487
Tanga, P., Carry, B., Colas, F., et al. 2015, MNRAS, 448, 3382
Taylor, G. E., & Dunham, D. W. 1978, Icarus, 34, 89
Tedesco, E. F., Noah, P. V., Noah, M., & Price, S. D. 2002, AJ, 123, 1056
Tedesco, E. F., Noah, P. V., Noah, M., & Price, S. D. 2004, NASA Planetary Data System, 12
Thomas, P. 1999, Icarus, 142, 89
Thomas, P. C., Binzel, R. P., Gaffey, M. J., et al. 1997, Science, 277, 1492
Torppa, J., Kaasalainen, M., Michalowski, T., et al. 2003, Icarus, 164, 346
Usui, F., Kuroda, D., Müller, T. G., et al. 2011, PASJ, 63, 1117
van Dam, M. A., Le Mignant, D., & Macintosh, B. A. 2004, Appl. Opt., 43, 5458
Vernazza, P., Zanda, B., Binzel, R. P., et al. 2014, ApJ, 791, 120
Viikinkoski, M., Kaasalainen, M., & Durech, J. 2015a, A&A, 576, A8
Viikinkoski, M., Kaasalainen, M., Durech, J., et al. 2015b, A&A, 581, L3
Wizinowich, P. L., Acton, D. S., Lai, O., et al. 2000, Adaptive Optical Systems Technology, Proc. SPIE, 4007, 2
Zielenbach, W. 2011, AJ, 142, 120
Zuber, M. T., Smith, D. E., Cheng, A. F., et al. 2000, Science, 289, 2097

Appendix A: Diameter and mass estimates from the literature

Diameter and mass estimates of (6) Hebe from the literature are presented here in Table A.1 and Fig. A.1 (diameter) and Table A.2 and Fig. A.2 (mass). Average values were determined following the method by Carry (2012), which consists in rejecting all the estimates that do not fall within one standard deviation of the average value, then by recomputing the average without these values.

Table A.1. Volume-equivalent diameter estimates of (6) Hebe gathered from the literature.

	Diameter (D, km)	Method	Reference
1	215.00 ± 21.50	STM	Morrison (1974)
2	$201.00 \pm 20 \times 10$	STM	Morrison (1977)
3	186.00 ± 9.00	Occ	Taylor & Dunham (1978)
4	$190.40 \pm 7 \times 10$	Occ	Dunham & Mallen (1979)
5	185.18 ± 2.90	STM	Tedesco et al. (2004)
6	180.42 ± 8.50	STM	Ryan & Woodward (2010)
7	214.49 ± 10.25	NEATM	Ryan & Woodward (2010)
8	180.00 ± 40.00	LC+Occ	Durech et al. (2011)
10	197.14 ± 1.83	STM	Usui et al. (2011)
11	185.00 ± 10.68	NEATM	Masiero et al. (2011)
12	165.00 ± 21.00	LC+AO	Hanuš et al. (2013)
13	195.64 ± 5.44	NEATM	Masiero et al. (2014)
	191.5 ± 8.3		Mean value*
	193 ± 6	ADAM (SPHERE only)	This paper
	196 ± 6	ADAM (all AO)	This paper
	$198 \pm 4/2$	TPM	This paper

Notes. STM: Standard Thermal Model, NEATM: Near-Earth Asteroid Thermal Model, LC: light curve, Occ: stellar occultation, AO: adaptative optics imaging, LC+Occ: light curve-based 3-D model scaled using an occultation, LC+AO: light curve-based 3D model scaled using adaptative optics images. (*) Using only values falling within 1σ of the average value of the full dataset.

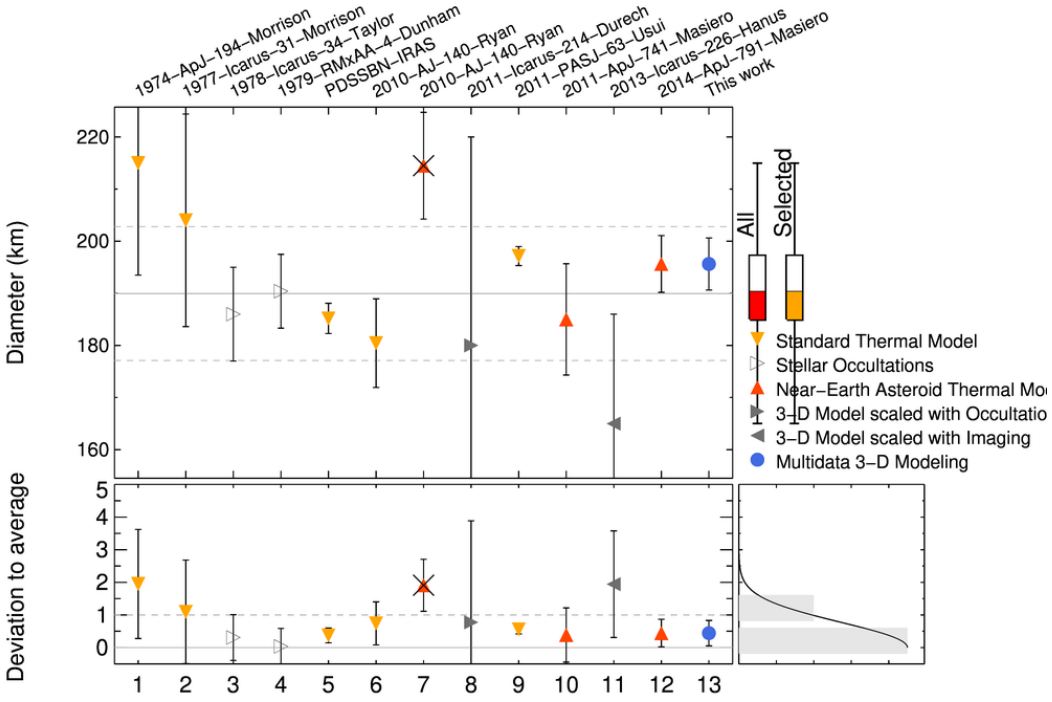

Fig. A.1. Diameter estimates of (6) Hebe gathered from the literature.

Table A.2. Mass estimates of (6) Hebe gathered from the literature.

	Mass (M, kg)	Method	Reference
1	$1.37 \pm 0.44 \times 10^{19}$	OD	Michalak (2001)
2	$1.37 \pm 0.18 \times 10^{19}$	OD	Kochetova (2004)
3	$1.28 \pm 0.06 \times 10^{19}$	OD	Baer & Chesley (2008)
4	$3.18 \pm 2.19 \times 10^{17}$	PE	Fienga et al. (2009)
5	$9.07 \pm 0.91 \times 10^{18}$	PE	Folkner et al. (2009)
6	$1.27 \pm 0.13 \times 10^{19}$	OD	Baer et al. (2011)
7	$1.41 \pm 0.24 \times 10^{19}$	PE	Fienga et al. (2011)
8	$1.34 \pm 0.33 \times 10^{19}$	PE	Konopliv et al. (2011)
9	$1.36 \pm 0.29 \times 10^{19}$	OD	Zielenbach (2011)
10	$1.55 \pm 0.18 \times 10^{19}$	OD	Zielenbach (2011)
11	$1.54 \pm 0.24 \times 10^{19}$	OD	Zielenbach (2011)
12	$1.53 \pm 0.34 \times 10^{19}$	OD	Zielenbach (2011)
13	$1.41 \pm 0.17 \times 10^{19}$	PE	Fienga et al. (2013)
14	$8.39 \pm 1.95 \times 10^{18}$	PE	Kuchynka & Folkner (2013)
15	$8.06 \pm 0.91 \times 10^{18}$	PE	Pitjeva (2013)
16	$8.95 \pm 0.60 \times 10^{18}$	OD	Goffin (2014)
17	$1.21 \pm 0.08 \times 10^{19}$	OD	Kochetova & Chernetenko (2014)
18	$1.86 \pm 0.13 \times 10^{19}$	PE	Fienga et al. (2014)
19	$1.58 \pm 0.19 \times 10^{19}$	PE	Fienga (priv. comm.)
	$1.31 \pm 0.24 \times 10^{19}$		Mean value*

Notes. OD: orbital deflection, PE: planetary ephemeris. (*) Using only values falling within 1σ of the average value of the full dataset.

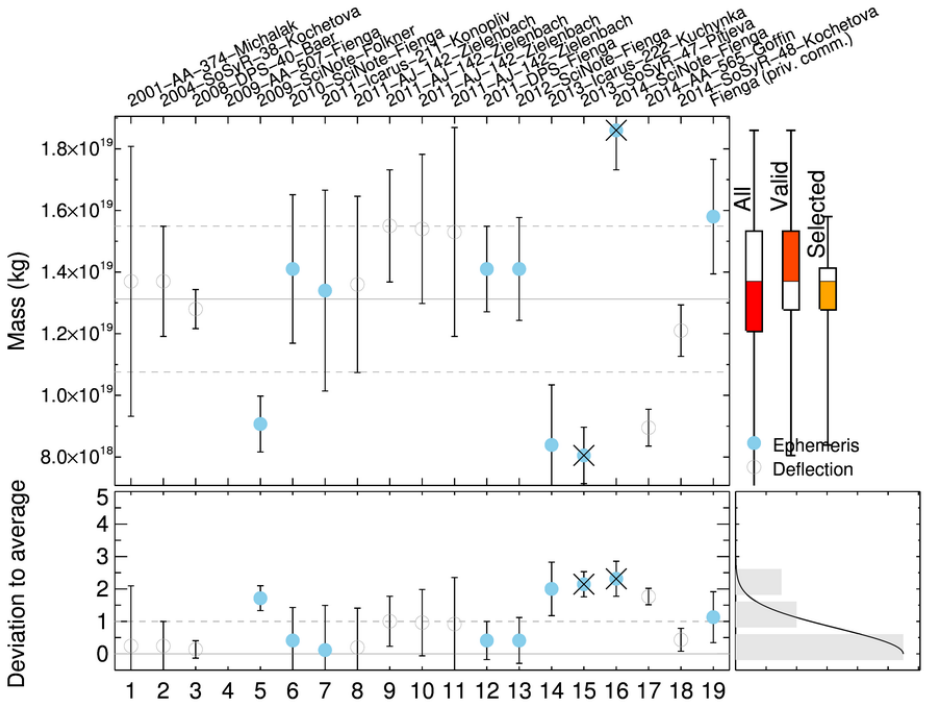

Fig. A.2. Mass estimates of (6) Hebe gathered from the literature.

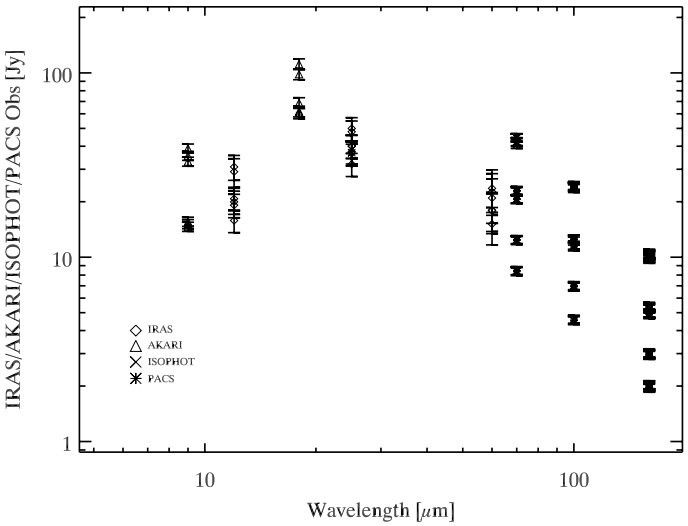

Fig. B.1. Thermal flux measurements of (6)-Hebe used for the thermophysical modeling. From IRAS (12, 25, 60, 100 μm, Tedesco et al. 2002), AKARI-IRC (9, 18 μm, Usui et al. 2011), ISO-ISOPHOT (25 μm, Lagerros et al. 1999), and *Herschel*-PACS (70, 100, 160 μm, Müller et al., in prep.).

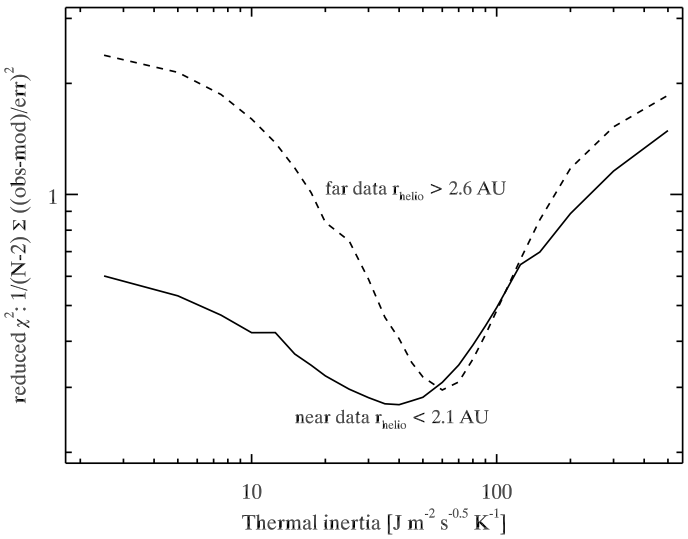

Fig. B.2. Thermal inertia of (6) Hebe derived from the thermophysical modeling. The overall preferred solution (lower reduced χ^2) is ~60 J m^{-2} s$^{-0.5}$ K^{-1} for data acquired at heliocentric distance $r < 2.1$ AU and ~40 J m^{-2} s$^{-0.5}$ K^{-1} for data taken at $r > 2.6$ AU. While this might be indicative of changing thermal inertia with temperature, one should be extremely cautious when interpreting this result, as a range of solutions cannot be ruled out based on the χ^2 values presented here.

Appendix B: Thermophysical model

The thermophysical model (TPM) used in this work predicts for a given set of parameters, including the volume-equivalent diameter D, albedo p_v, surface roughness $\bar{\theta}$, and thermal inertia Γ, a flux that can be compared to the observed flux. The input parameters can then be optimized by minimizing the reduced χ^2 between the model and observations. Thermal measurements of Hebe used in the modeling procedure are plotted in Fig. B.1.

Here, a solution was derived simultaneously for Γ, D and p_v for a range of different $\bar{\theta}$ knowing Hebe's absolute magnitude H and magnitude slope G. Different emissivity models, including constant $e = 0.9$ and wavelength-dependent emissivities, were tested. We adopted the emissivity model for large main-belt asteroids of Müller & Lagerros (1998) which was found to provide the most satisfactory results (lower χ^2). Finally, best-fit solutions were found for significant surface roughness and Γ values ranging from 20 to 100 J m^{-2} s$^{-0.5}$ K^{-1} (Fig. B.2). The resulting observation-to-model flux ratios are shown at Fig. B.3.

We further used a well established method (Gundlach & Blum 2013) to determine the grain size of the surface regolith of Hebe. The method consists in estimating the heat conductivity of the surface material derived from the thermal inertia measurements and then to compare the values with calculations of the heat conductivity of a model regolith for distinct volume-filling factors of the regolith grains. The thermal inertia value and the surface temperature of these bodies are two input parameters for the method. First of all the thermal inertia Γ is used to calculate the conductivity κ using:

$$\kappa = \frac{\Gamma^2}{\phi \rho c}, \tag{B.1}$$

where c is the specific heat capacity, ρ the material density, and ϕ the regolith volume-filling factor, which is typically unknown.

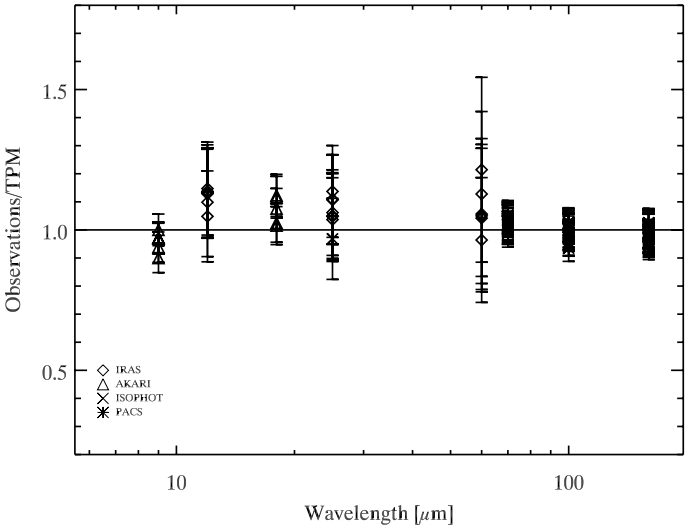

Fig. B.3. Observation-to-model flux ratios as a function of wavelengths, based on color-corrected mono-chromatic flux densities and the corresponding TPM flux predictions.

So, this last parameter is varied between 0.6 (close to the densest packing of equal-sized particles) and 0.1 (extremely fluffy packing, plausible only for small regolith particles) with $\Delta\phi = 0.1$, while here we take values for ρ and c typical of H5 ordinary chondrites from Opeil et al. (2010). We estimate Hebe's temperature to be 230 K and 180 K for the thermal inertia determination at 1.94 and 2.87 AU, respectively.

By doing so, we find a typical grain size of 0.2–0.3 mm (Figs. B.4 and B.5).

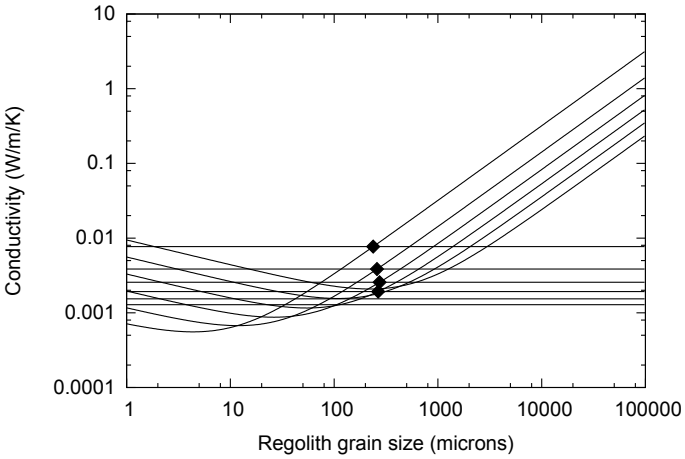

Fig. B.4. Hebe's regolith grain size. Horizontal lines indicate the derived values of the heat conductivity, following Eq. (B.1), for the different volume-filling factors of the material and for a thermal-inertia value of 40 J m^{-2} s$^{-0.5}$ K^{-1} and a surface temperature of 180 K. The curves represent the thermal conductivity of a regolith with thermophysical properties of a H5 meteorite as from Opeil et al. (2010) as a function of the regolith grain size. The intersection of the curves with the horizontal lines gives the grain size of the regolith.

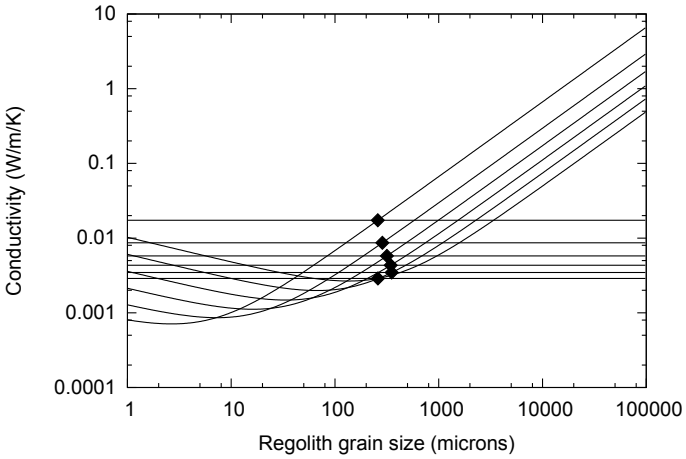

Fig. B.5. Same as Fig. B.4 but showing the regolith grain size for the a thermal inertia of 60 J m^{-2} s$^{-0.5}$ K^{-1} and a surface temperature of 230 K.